Evaluation of a Potential Flow Model for Propeller and Wind Turbine Design

Scott M. Palmiter* and Joseph Katz†
San Diego State University, San Diego, California 92119

A three-dimensional, potential flow based, unsteady panel code was used to model the flow over rotating propeller blades. It is assumed that for best performance, flow separations must be avoided on the rotating blades of propellers and wind turbines. In this case, idealized tools such as the one used here are significantly faster and simpler for calculating the surface pressure distribution and the resulting performance parameters. Similar experimental data on the surface pressures and on common performance parameters are widely available on propellers (and less on wind turbines) and, therefore, the validation was performed on a two-blade NACA propeller. In the first part of this study, computed results were validated and were found to compare favorably with the experimental data for a wide range of performance parameters. In the second part of this study, a rotor optimization is performed using a generic rotor blade shape. For simplicity, a rectangular blade with several taper ratios and linear twist was used. The computed results indicate that even with this simple geometry, a more efficient design (than the baseline) is possible. It is concluded therefore that by using this tool more complex blade shapes and customized airfoil sections can be developed, leading to additional improvements in performance and efficiency.

Nomenclature

$c(r)$	=	propeller (blade) chord
C_P	=	propeller power coefficient
C_{pk}	=	panel k pressure coefficient
C_T	=	propeller thrust coefficient
D	=	propeller diameter
F_k	=	force on panel k
J	=	advance ratio [see Eq. (12)]
l, m, n	=	local panel coordinates
M	=	total number of surface panels
N	=	revolutions per second
n	=	unit vector normal to surface
P	=	power required to rotate propeller
R	=	propeller radius
r	=	radial distance along blade
S_k	=	area of panel k
T	=	propeller thrust
Tq	=	propeller torque
U_{ref}	=	local velocity [see Eq. (6)]
U_∞	=	propeller forward velocity
x, y, z	=	Cartesian coordinate system
η	=	propeller efficiency
λ	=	blade taper ratio (tip chord/root chord)
μ	=	panel doublet strength
ρ	=	air density
σ	=	panel source strength
Φ	=	velocity potential
Ω	=	propeller rotations, rad/s

I. Introduction

THE flow over rotors is complicated by the circular motion of the blades and by the strong interaction with the wake. Therefore, the ability to calculate the pressure distribution and the resulting loads on the blades is even more important than in the case of an airplane wing. An account of the various rotor/propeller modeling techniques is provided in reviews such as [1–3]. These studies focused more on the helicopter rotor problem where in addition to the complex wake interaction, the flowfield is complicated by the interaction with the body and by the unsteady loads due to the forward flight of the flapping blade. In case of propellers and wind turbines the flow is less complex and with proper modeling of the fully developed wake, queasy steady-state methods can be used. Early propeller development relied more on experimental methods [4] while a survey of more recent models, focused on wind turbine performance is found in [5]. The main conclusion is that for such high Reynolds number flows, current CFD methods are limited and very large grids are required. One of the main problems is that the spiral wake has a strong effect on the rotor flow and therefore a large computational domain (including the far wake) is required. The problem is complicated by the wake vortex decay in finite difference/element CFD methods, reducing their accuracy for this particular application (not to mention several days of computation time for each point). On the other hand, the objective of a good rotor design is to obtain attached flow over the whole rotor and these conditions are well modeled by potential flow [6–8]. Because there is no vorticity decay in the wake, this type of wake interaction is well predicted. Another advantage of the present three-dimensional model is that the unknowns are distributed on the rotor surface and not in the whole computational domain, as in finite difference or finite element methods. This reduction in the computational effort, results in reduced computational times by several orders of magnitude.

II. Basic Features of the Numerical Model

The method used here (called *panel method*) is based on solving the Laplace equation using the surface singularity distributions ([6]) and its advantage, compared with the finite difference (or finite volume) approach, is that the unknown elements are distributed on the surface and not in the whole fluid volume, thereby significantly reducing computational effort. Another advantage is that the velocity field is obtained by solving the continuity equation only (decoupled from the momentum equation), and instead of three velocity components at each point only one unknown, namely the velocity potential, is sought. So in conclusion, these methods are very efficient numerically (requiring several orders of magnitude less computations) but applicable only to inviscid, attached flows.

*Graduate Student, Department of Aerospace Engineering and Engineering Mechanics. Member AIAA.

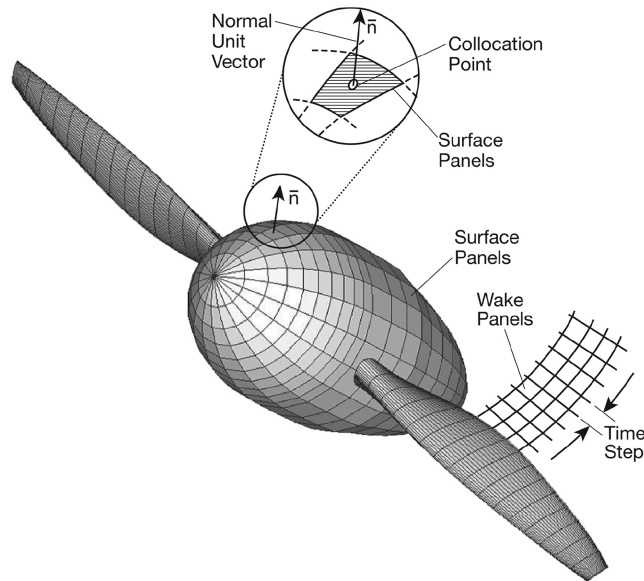†Professor, Department of Aerospace Engineering and Engineering Mechanics. Associate Fellow AIAA.

Fig. 1   Schematic description of the potential flow model.

The theoretical background of such panel methods is described schematically in Fig. 1. In this case the solid surface of the moving body is subdivided to panel elements, as shown. The velocity field in the fluid surrounding the rotor is obtained by solving the incompressible continuity equation

$$\nabla^2 \Phi = 0 \qquad (1)$$

where Φ is the velocity potential in a stationary inertial frame of reference. The boundary conditions require that the normal component of velocity on the solid boundaries of the body must be zero (see the unit normal vector **n** shown in Fig. 1). Of course this condition must be met at all the surface nodes called collocation points. Since the gradient of the velocity potential normal to a solid surface is zero, the potential enclosed by the body must be constant. Therefore, an alternate form of this boundary condition, called the Dirichlet condition, requires that the potential inside a closed body be constant. By setting the constant to zero this boundary condition becomes

$$\Phi_i = 0 \qquad (2)$$

The present method is based on this simpler boundary condition and in principle, this condition is met at all collocation points, below (or inside) the solid surface. Solution of Eq. (1) provides the velocity field through the whole fluid domain. The pressures and corresponding fluid dynamic loads are then calculated separately by using the Bernoulli equation (recall that the continuity and momentum equations are not coupled for ideal flows).

The numerical solution begins with a surface grid of M elements (called panels), as shown in Fig. 1 and for each panel a constant strength singularity distribution (of sources and doublets) is assumed. Next, for each collocation point the potential due to all elements must add to zero inside the body (recall that the collocation point is assumed to be on the inner surface of the body). Consequently, when Eq. (2) is specified at one collocation point, it represents the added influence of all j panel elements (including the wake, which is modeled by thin doublet surfaces)

$$\sum_{k=1}^{M} B_{jk}\sigma_k + C_{jk}\mu_k = 0 \qquad (3)$$

This equation basically states that the potential at the collocation point of panel k is the sum of the incremental potentials of all the surface panels (and the source strength σ_k is known from the freestream conditions; see [6]). This equation is then applied to all M collocation points with the M unknowns doublets μ_k, thus reducing Eq. (1) into a set of linear algebraic equations (matrix of order M). By solving the M equations the unknown doublets for each panel are calculated and therefore the potential Φ is known everywhere.

In the current mode, a time stepping solution is used where a new row of wake panels is shed from the blades trailing edges at each time step (see Fig. 2). The wake model, after four revolutions is also shown at the lower corner of the figure. Once Eq. (3) is solved (at each time step) the unknown singularity values μ_k are obtained and the local velocity components can be evaluated at each panel in terms of the panel local coordinates (l, m, n) as

$$q_l = -\frac{\partial \mu}{\partial l}, \qquad q_m = -\frac{\partial \mu}{\partial m} \qquad (4)$$

Note that the normal velocity (in the n direction) is automatically zero. Once the velocity is calculated (and the freestream velocity is added) the surface pressure and resulting forces can be calculated, using the Bernoulli equation. In terms of the pressure coefficient it has the form

$$C_{pk} = 1 - \frac{q^2}{U_{\text{ref}}^2} + \frac{2}{U_{\text{ref}}^2}\frac{\partial \Phi}{\partial t} \qquad (5)$$

This is a time-dependent formulation but at the present time the second (time dependent) term decays after the wake is fully developed. The reference velocity U_{ref} is the kinematic velocity at each panel (at a distance r from the rotation axis)
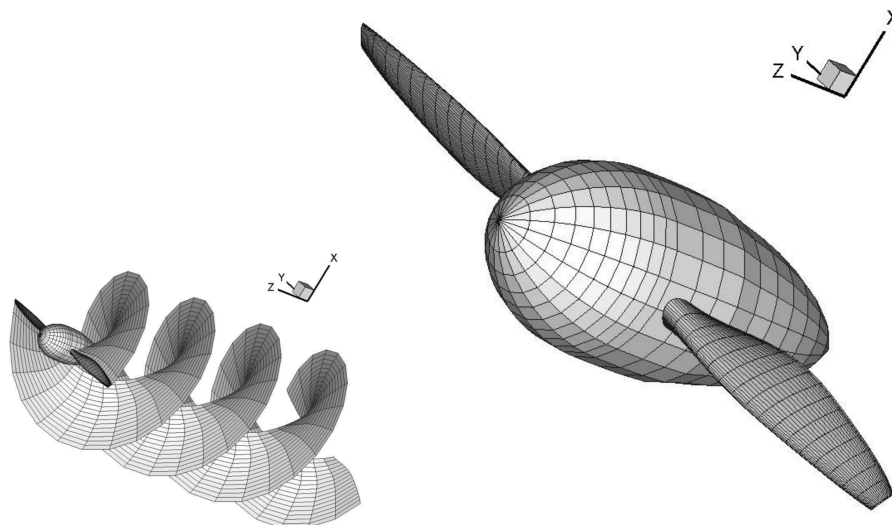

Fig. 2   The surface panel model of the Clark Y 5868–9 propeller, and the spiral wake, after four and a half rotations.

$$U_{ref} = U_\infty + r\Omega \qquad (6)$$

Note that this is a vector relation and U_∞ is the forward velocity into the z direction (see Fig. 2) and Ω is the rotation about the z axis. The force on a panel of area S_k is then

$$F_k = -C_{pk}(0.5\rho U_{ref}^2)S_k n_k \qquad (7)$$

and the direction is given by the vector n_k. Adding up the loads of all panels in the advancing direction is the thrust T, and in the tangential direction (multiplied by r) yields the torque Tq. The power P is then simply the torque times the rotation speed (N represents revolutions per second)

$$P = Tq \cdot \Omega = Tq \cdot 2\pi N \qquad (8)$$

The thrust C_T, and power C_P coefficients are defined as

$$C_T = \frac{T}{\rho N^2 D^4} \qquad (9)$$

$$C_P = \frac{P}{\rho N^3 D^5} \qquad (10)$$

and D is the propeller diameter. The efficiency η is the work of the propeller thrust divided by the work done by the torque

$$\eta = \frac{TU_\infty}{P} = \frac{C_T}{C_P}\frac{U_\infty}{ND} = \frac{C_T}{C_P}J \qquad (11)$$

and here J is the advance ratio

$$J = \frac{U_\infty}{ND} \qquad (12)$$

III. Comparison of Computed Results with Experimental Data

The above described numerical model is validated against the experimental data presented in [4]. The two-bladed propeller is based on a Clark Y airfoil section and the radial variations of thickness and pitch are shown in Fig. 3. The blade pitch is defined as the relative blade angle at $r/R = 0.75$. In this study two condition were considered : a) pitch of 25 deg, and b) pitch of 35 deg. More details on the geometry are provided in [4], along with integral performance data versus advance ratio (as it will be shown later).

The computational grid of the propeller is shown in Fig. 2, and each propeller blade was modeled by 832 surface panels and for the hub, 400 panels were used. This panel density was found to be sufficient for calculating the pressure distribution and resulting performance parameters. At the lower part of Fig. 2, the wake panels are shown after four and a half rotations. In this case the wake is rigid (e.g., not deforming) which is a sufficient approach for the high advance ratio case (as shown). For the present computations, the propeller was rotating and moving forward until a fully developed wake and the corresponding force coefficients were obtained. Clearly for the low advance ratios, a larger number of revolutions was required, because of the strong interaction with the spiral wake.

An important outcome of the analytical/numerical modeling is the detailed pressure distributions on the rotating blade. Such data is presented at four radial stations in Fig. 4, for an advance ratio of $J = 0.7$. The shape of the local airfoil section and orientation is also shown in this figure. For example, near the root (at $r/R = 0.40$) the pressure distribution is well behaved (no sharp adverse pressure gradient) and flow separation is unlikely. Toward the rotor tip the suction peak at the leading edge increases, resulting in less than ideal pressure distribution. This could be cured by changing the local airfoil shape and by adding more camber (e.g., by drooping the leading edge). In conclusion, the pressure distribution can be used to custom-design airfoil shapes for a particular blade geometry. It also can be used to identify potential areas of flow separation (with sharp suction peaks, etc.) so that these conditions can be avoided.
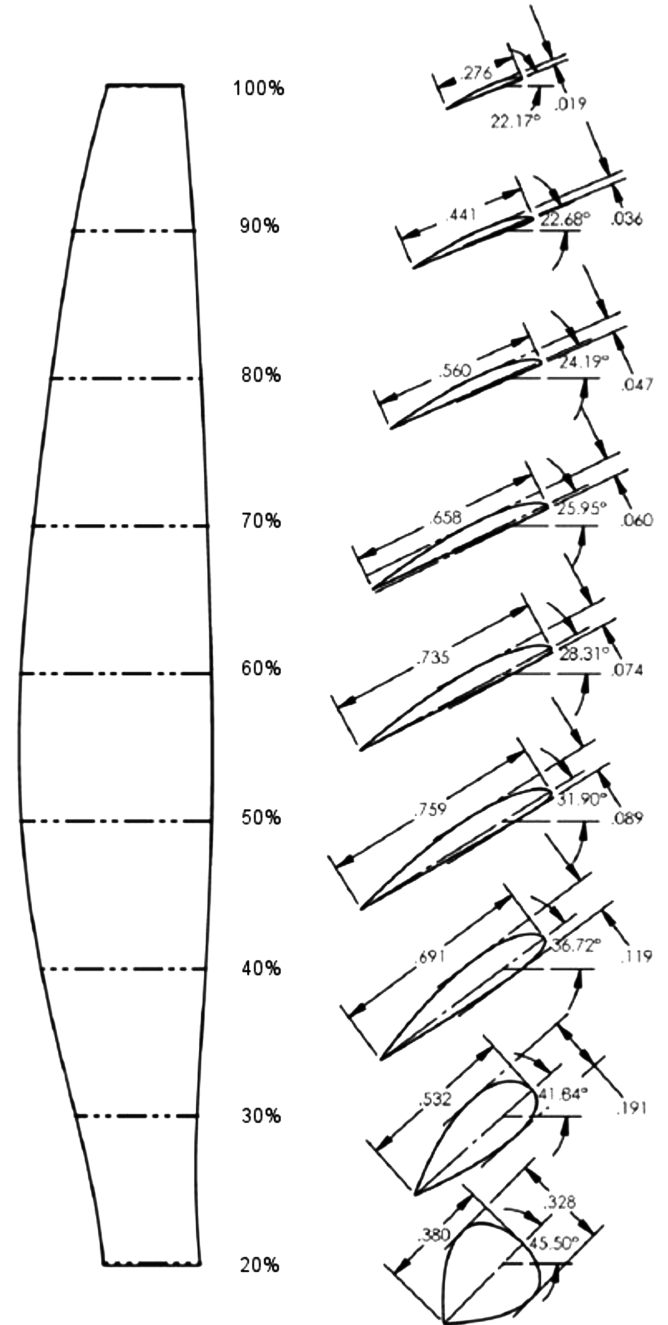

Fig. 3 Geometry of the propeller blade used to validate the numerical model (pitch = 25 deg). Blade root is at $r/R = 0.20$.

Integration of the chordwise pressure distributions, as shown in Fig. 4 provides the local components of the thrust and torque. The radial (along the blade) thrust distribution is similar to the spanwise loading on a wing and has an impact on both structural and efficiency related considerations. Contrary to most wings, the highest loading is towards the tip, as shown in Fig. 5. This is of course a result of the higher velocity vector due to the propeller rotation. At the tip, as in the case of a finite wing, the loading drops to zero because no pressure difference can be maintained between the upper and lower blade surfaces.

Figure 5 shows the radial loading for three advance ratios and the relative loading increases with reduced advance ratio. This is explained by the velocity diagram in Fig. 6. Assuming a constant rotation, the local tangential velocity is fixed at $r\Omega$. The relative angle of attack (due to the resultant U_{ref}) will increase with reduced forward speed U_∞, or with reduced advance ratio [see Eq. (12)]. Consequently, the thrust coefficient will also increase with reduced advance ratio as shown in Fig. 7. A similar effect is expected when

a) $r/R = 0.4$

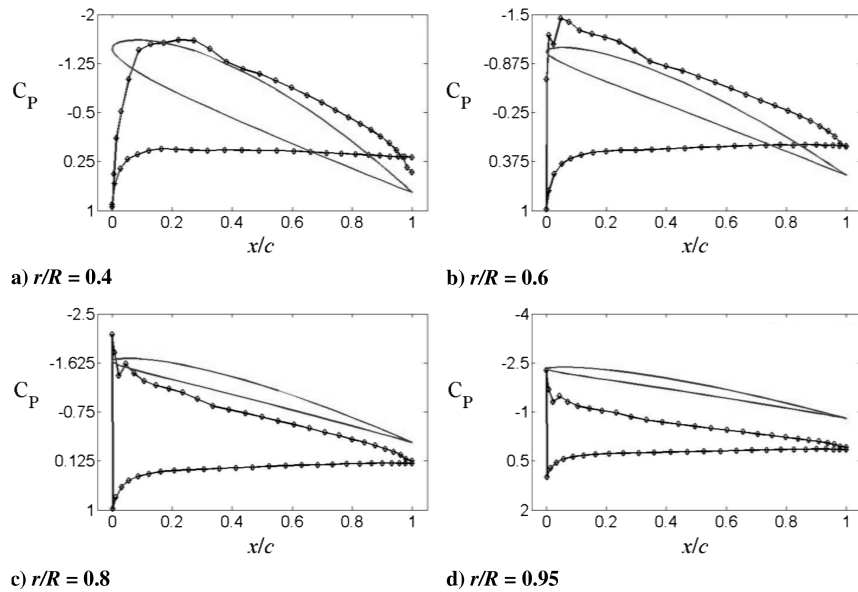
b) $r/R = 0.6$

c) $r/R = 0.8$

d) $r/R = 0.95$

Fig. 4 Section pressure distributions at several radial stations. The blade shape and orientation is shown schematically by the inset. $J = 0.7$ and pitch = 25 deg.
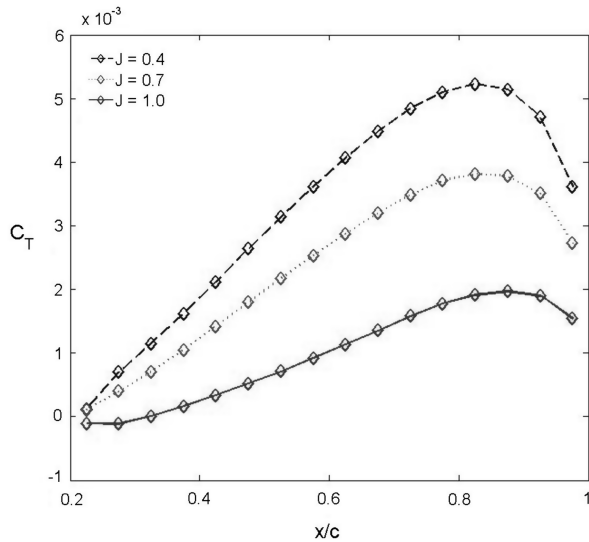

Fig. 5 Radial loading along the blade for several advance ratios. Pitch = 25 deg.
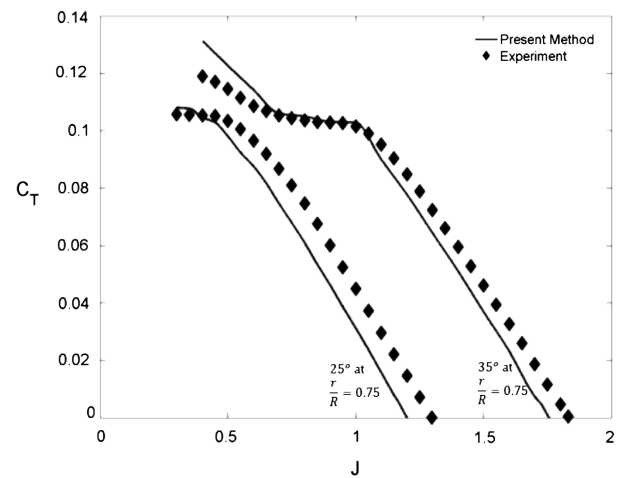

Fig. 7 Thrust coefficient versus advance ratio for the Clark Y 5868–9 propeller.
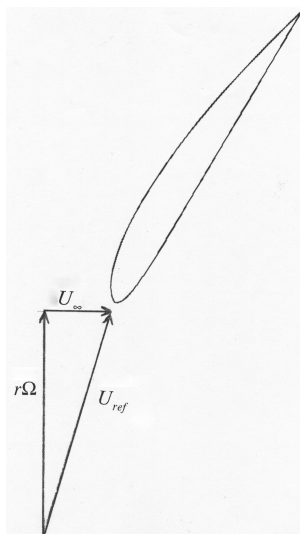

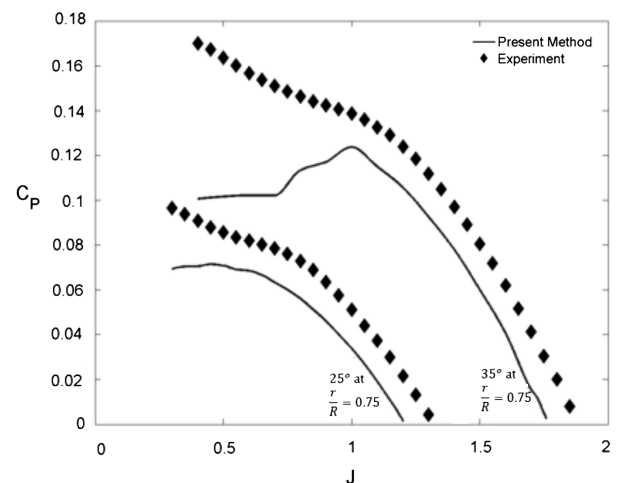Fig. 6 Velocity diagram for a generic radial blade station.

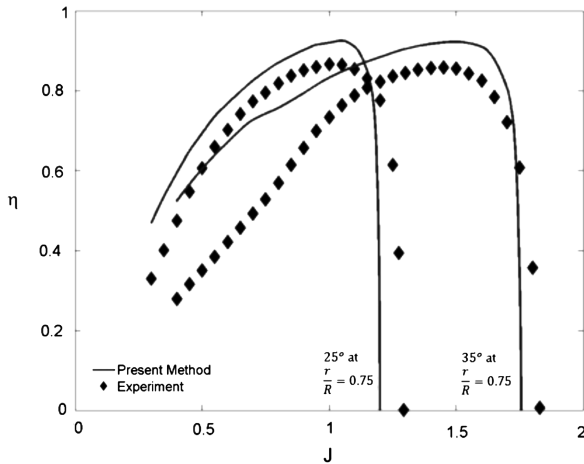Fig. 8 Power coefficient versus advance ratio for the Clark Y 5868–9 propeller.

Fig. 9   Efficiency versus advance ratio for the Clark Y 5868–9 propeller.

the blade pitch is increased from 25 to 35 deg, as shown in the figure. The computed trends are in good agreement with the experimental results. It is interesting to note that the experimental thrust coefficient is higher than the one predicted by the ideal flow, but this is a result of the rigid wake used for the computations. Deforming wake mode was not used for this validation simply to reduce computational times, resulting in the wake not leaving exactly parallel to the trailing edge (thereby reducing the local circulation). Future validations are planned using deforming wake routines. Another interesting wake effect is seen in Fig. 7, for the low advance ratios. As the forward speed U_∞ is reduced (and the advance ratio is reduced) more rotations are required to develop the wake influence. For example , at

an advance ratio of 0.4, at least 10 full rotations are needed to stabilize the calculated thrust values.

Another interesting trend in Fig. 7 is the drop in the experimental thrust coefficients for the low advance ratios, at pitch = 35 deg. This is a result of flow separation and the ideal calculations showed pressure coefficients in excess of -12.00 near $r/R = 0.75$, clearly signaling the likelihood of flow separations. This example demonstrates how potential flow calculations can be used to identify conditions that must be avoided (in order to avoid flow separations).

Instead of the torque, the equivalent power coefficient shown in Fig. 8 is presented. This coefficient is expected to follow a trend similar to the thrust coefficient, because a wing's drag (in attached flow) increases with its lift (thrust in this case). The reduction in power (and torque) at the lower advance ratios (particularly for the 35 deg pitch case) is more pronounced and of course it is due to flow separation resulting from the increased local blade angle of attack (see Fig. 6).

The overall efficiency is shown in Fig. 9 for the two pitch values and the computed results agree quite well with the experimental data. As expected, at the low advance ratios, the experimental efficiency is significantly lower due to the earlier mentioned flow separation, mainly for the 35 deg pitch case. Also, with increasing advance ratio, the blade angle of attack is reduced (see Fig. 6), the thrust is reduced, and the efficiency drops sharply as seen in Fig. 9.

IV.   Generic Propeller Blade Optimization

The previous validation clearly indicates that at advance ratio of less than $J < 1$ the propeller with the 35 deg pitch loses efficiency due to local flow separations. Also, throughout the whole range, the calculated pressure distributions indicate less than ideal conditions for large portions of the blade. This suggest that by changing the blade geometry significant improvements can be achieved (and in
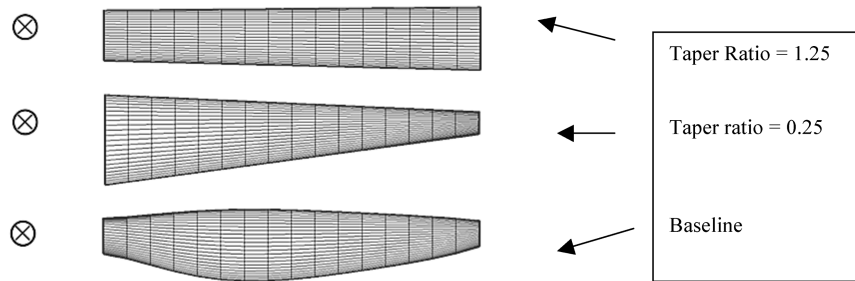

Fig. 10   Shape of the generic propeller next to the baseline design. The circle at the left represents the center of rotation. The blade base is at $r/R = 0.20$.
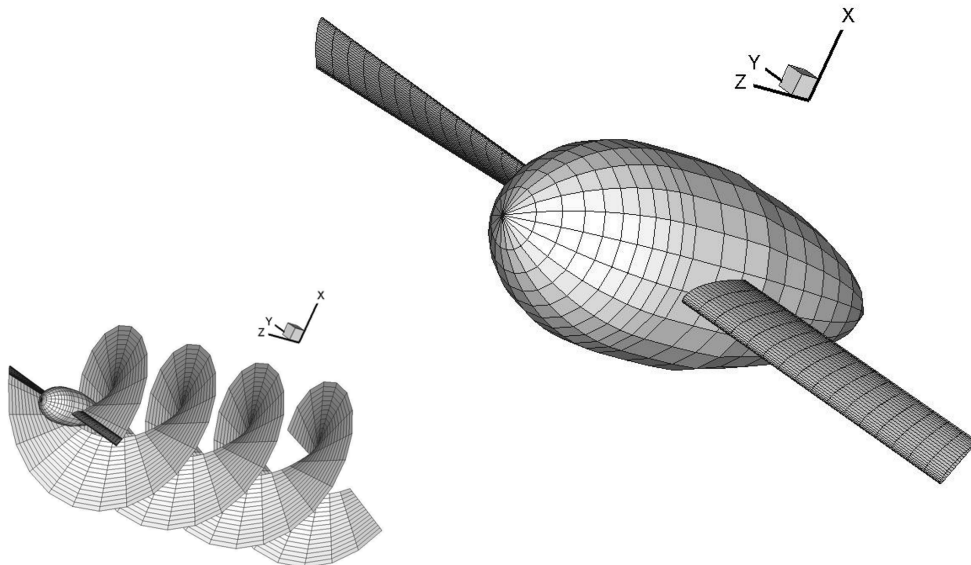

Fig. 11   The surface panel model of the generic propeller ($\lambda = 1.00$) and the spiral wake, after four and a half rotations.
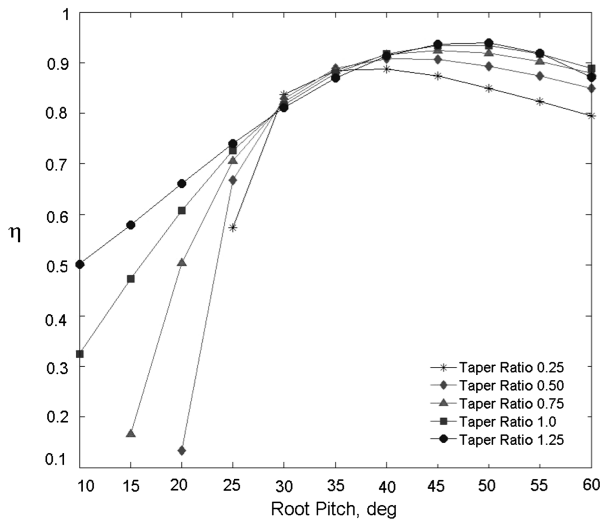
Fig. 12 Variation of efficiency versus the optimization parameters for 25 deg pitch at $J = 1.00$.

practice the expected range of advance ratio must be quite narrow). The potential of using this method for such propeller development is demonstrated by the following simple geometry optimization. Thus, the main objective here is to demonstrate that even with a simple geometry, improvements over the baseline propeller are possible. For simplicity, a rectangular blade shape was used, retaining the baseline blade Clark Y airfoil geometry (of [4]). Thickness ratio varied linearly between 20% at the blade root, to 9% at the tip. Only two variables (taper and twist) were used for this brief optimization. The pitch varied linearly between the root ($r/R = 0.20$) and the tip ($r/R = 1.00$) within the range of 20–70 deg, and taper ratio varied between 0.25 and 1.25. The taper ratio λ was defined as the ratio between the tip chord $c(R)$ and the root chord $c(r = 0.20R)$

$$\lambda = \frac{c(R)}{c(r = 0.20R)} \qquad (13)$$

The shapes of the maximum and minimum taper ratios next to the baseline blade shape are shown in Fig. 10.

The panel model used for the optimization was similar (same number of panels) to the baseline model and is shown in Fig. 11. The

blade pitch was defined as before, based on the chord angle at radial station $r/R = 0.75$. Computations were performed for both blade pitch of 25 and 35 deg, and results for the efficiency at $J = 1.00$ are presented in Fig. 12 (for pitch = 25 deg). For this example, five taper ratios and 11 twist variations were computed. The abscissa in this figure shows the various blade twist tested and the best efficiency (for blade pitch of 25 deg) appears to fall near taper ratio of 1.0 and radial twist of about 50 deg.

Note that the radial velocity increases with the radial distance r and, therefore, the larger taper ratios will have larger thrust (and larger torque). After evaluating the performance over a wide range, the propeller with the taper ratio of $\lambda = 0.75$ and radial twist variation of 29 deg (root pitch = 45 deg, tip pitch = 16 deg) was selected (for the case of 25 deg blade pitch).

To evaluate the improvement in the shape of the pressure distributions, the computed results for the optimized blade are shown in Fig. 13 (for $J = 0.7$). The shape of the local airfoil section and orientation is also shown in this figure. Comparison with the computed data in Fig. 4 shows less leading edge suction and more moderate pressure distribution, suggesting that separation is less likely (speculating about the nature of the boundary layer; see [9]).

The integrated chordwise pressure distributions, (as in Fig. 4) for the best in the group blade is shown in Fig. 14. As in the previous case, the loading increases toward the larger radial position, but ends with zero at the tip. This is again due to the fact that at the tip, no pressure difference can be maintained between the upper and lower blade surfaces.

One of the more important features of the radial loading plot is the ability to compare the two propeller designs. This is presented for three advance ratios in Fig. 15, and the data for the baseline propeller is transferred from Fig. 5. In all three cases (of advance ratios) the modified propeller generates more thrust at a smaller radius, thereby reducing the torque and increasing efficiency (this is equivalent to a better spanwise loading on a high aspect ratio wing). Furthermore, generating larger loads at smaller radial distance translates to structural and weight saving advantages (for the same thrust).

Based on Fig. 15, better performance is expected from the optimized (best in group) propeller shape. This is demonstrated in the following three figures, showing the thrust and power coefficients and the propeller efficiency.

Figure 16 shows the comparison between the two computed and the experimental thrust coefficient. The advantage of the new design is visible throughout the whole range of advance ratios and even more so for blade pitch of 35 deg. Other features of this figure are similar to the earlier discussion related to Fig. 7.

a) $r/R = 0.4$
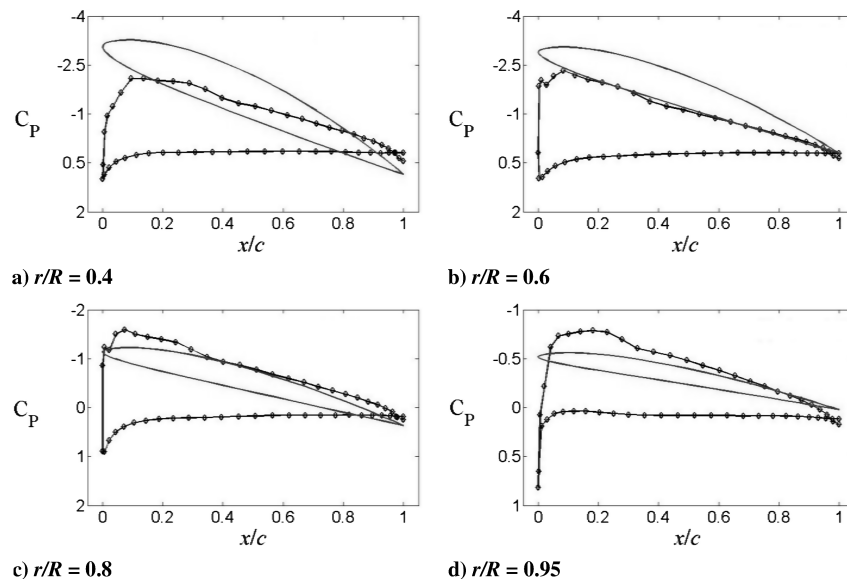
b) $r/R = 0.6$

c) $r/R = 0.8$

d) $r/R = 0.95$

Fig. 13 Section pressure distributions at several radial stations for the optimized blade shape. The blade shape and its orientation is shown schematically by the inset. $J = 0.7$ Pitch = 25 deg.
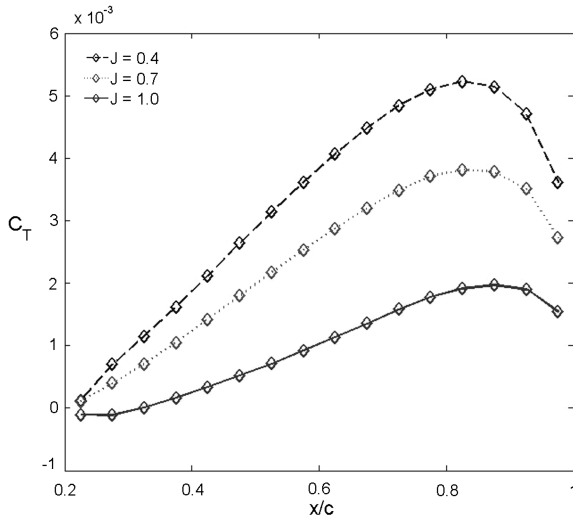
Fig. 14 Radial loading along the idealized blade for several advance ratios. Pitch = 25 deg.

The power coefficient comparison in Fig. 17 exhibits similar behavior and the new blade design appears to perform better. The large deviation between the calculated and experimental data beyond $J = 1$ (for pitch = 35 deg) is the result of flow separation during the experiment, as discussed with reference to Fig. 8.
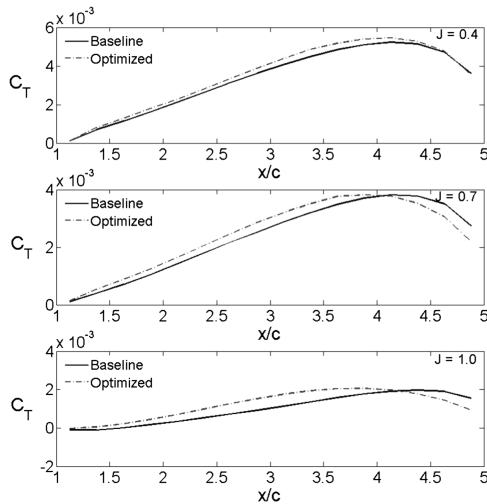

Fig. 15 Comparison of radial loading along the blade between the baseline and the taper ratio 0.75 design.
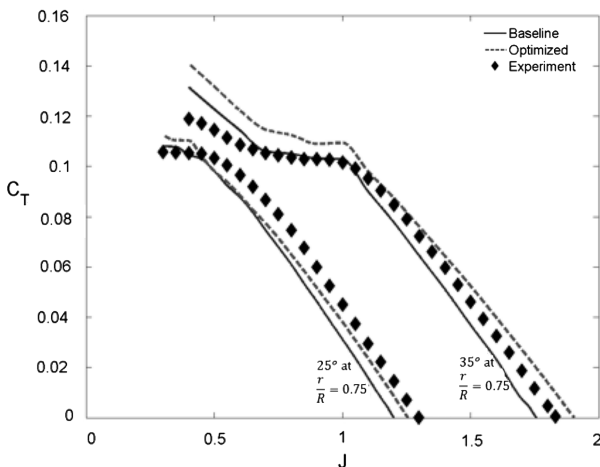

Fig. 16 Thrust coefficient versus advance ratio for taper ratio 0.75.
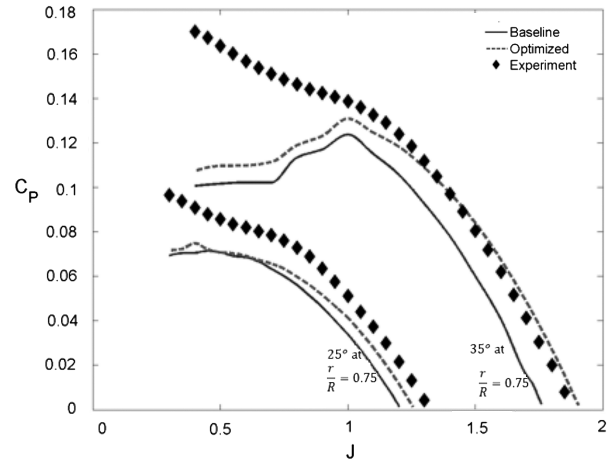

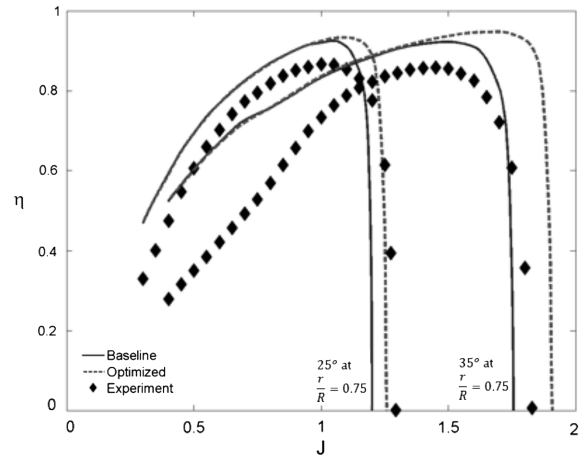Fig. 17 Power coefficient versus advance ratio for taper ratio 0.75.

Fig. 18 Efficiency versus advance ratio for taper ratio 0.75.

Finally, the overall propeller efficiency is plotted in Fig. 18. The agreement with the experimental data (for the baseline propeller) is quite good and the new propeller design shows a major increase in efficiency at the higher advance ratios. This in general is a result of slightly larger blade angle of attack in the modified design.

V. Conclusions

An existing panel code was modified so that propeller and wind turbine flows can be studied. The validation conducted here clearly indicates that the calculated chordwise pressure distribution can identify areas for possible flow separation, leading to more efficient (attached flow) designs. The method is much faster than other CFD tools and accounts for wake effects without vortex decay. A simple optimization routine demonstrated that improvement in propeller design can be achieved using this model. For best results, better airfoil shapes and more customized twist and blade shape can be developed.

References

[1] McCroskey, W. J., "Wake Vortex System of Helicopters," AIAA Paper 95-0530, Reno, NV, January 1995.
[2] Landgrebe, A. J., "New Directions in Rotorcraft Computational Aerodynamics Research in the, U. S.," *Proceedings of the AGARD 75th Fluid Dynamics Panel Symposium on Aerodynamics and Aeroacoustics of Rotorcraft*, Berlin, Germany, Oct. 1994.
[3] Nathan, H., and Sankar, L. N., "A Review of Computational Techniques for Rotor Wake Modeling," *38th AIAA Aerospace Sciences Meeting*, AIAA Paper 00-0114, 2000.
[4] Hartman, E. P., and Biermann, D., "The Aerodynamic Characteristics of Full-Scale Propellers Having 2, 3, and 4 Blades of Clark Y and R. A. F. 6

Airfoil Sections," NACA, T. R. No. 640, 1938.

[5] Gordon, J. L., "Challenges in Modeling the Unsteady Aerodynamics of Wind Turbines," *21st ASME Wind Energy Symposium and the 40th AIAA Aerospace Sciences Meeting*, American Society of Mechanical Engineers Paper 2002-0037, 2002.

[6] Katz, J., and Maskew, B., "Unsteady Low-Speed Aerodynamic Model for Complete Aircraft Configurations," *Journal of Aircraft*, Vol. 25, No. 4, 1988, pp. 302–310.
doi:10.2514/3.45564; also AIAA Paper No. 86-2180, Aug. 1986.

[7] Ashby, L. D., Dudley, M. D., Iguchi, S. K., Browne, L., and Katz, J., "Potential Flow Theory and Operation Guide for the Panel Code PMARC," NASA TM 102851, March 1990.

[8] Yon, S., Katz, J., and Ashby, D., "Unsteady Fluid Dynamic Model for Propeller Induced Flow Fields," AIAA Paper No. 91-1664, June 1991.

[9] Hufford, G. S., Drela, M., and Kerwin, J. E., "Viscous Flow Around Marine Propellers Using Boundary Layer Strip Theory," *Journal of Ship Research*, Vol. 38, No. 1, March 1994, pp. 52–62.